J. Fluid Mech. (2014), *vol.* 757, *pp.* 231–250.
doi:10.1017/jfm.2014.480

Flexibility in flapping foil suppresses meandering of induced jet in absence of free stream

Sachin Y. Shinde[1,‡] **and Jaywant H. Arakeri**[1,†]

[1]Department of Mechanical Engineering, Indian Institute of Science, Bangalore 560012, India

(Received 30 January 2014; revised 30 July 2014; accepted 16 August 2014;
first published online 19 September 2014)

Thrust-generating flapping foils are known to produce jets inclined to the free stream at high Strouhal numbers $St = fA/U_\infty$, where f is the frequency and A is the amplitude of flapping and U_∞ is the free-stream velocity. Our experiments, in the limiting case of $St \to \infty$ (zero free-stream speed), show that a purely oscillatory pitching motion of a chordwise flexible foil produces a coherent jet composed of a reverse Bénard–Kármán vortex street along the centreline, albeit over a specific range of effective flap stiffnesses. We obtain flexibility by attaching a thin flap to the trailing edge of a rigid NACA0015 foil; length of flap is $0.79\,c$ where c is rigid foil chord length. It is the time-varying deflections of the flexible flap that suppress the meandering found in the jets produced by a pitching rigid foil for zero free-stream condition. Recent experiments (Marais *et al.*, *J. Fluid Mech.*, vol. 710, 2012, p. 659) have also shown that the flexibility increases the St at which non-deflected jets are obtained. Analysing the near-wake vortex dynamics from flow visualization and particle image velocimetry (PIV) measurements, we identify the mechanisms by which flexibility suppresses jet deflection and meandering. A convenient characterization of flap deformation, caused by fluid–flap interaction, is through a non-dimensional 'effective stiffness', $EI^* = 8\,EI/(\rho\, V_{TE_{max}}^2\, s_f\, c_f^3/2)$, representing the inverse of the flap deflection due to the fluid-dynamic loading; here, EI is the bending stiffness of flap, ρ is fluid density, $V_{TE_{max}}$ is the maximum velocity of rigid foil trailing edge, s_f is span and c_f is chord length of the flexible flap. By varying the amplitude and frequency of pitching, we obtain a variation in EI^* over nearly two orders of magnitude and show that only moderate EI^* $(0.1 \lesssim EI^* \lesssim 1)$ generates a sustained, coherent, orderly jet. Relatively 'stiff' flaps $(EI^* \gtrsim 1)$, including the extreme case of no flap, produce meandering jets, whereas highly 'flexible' flaps $(EI^* \lesssim 0.1)$ produce spread-out jets. Obtained from the measured mean velocity fields, we present values of thrust coefficients for the cases for which orderly jets are observed.

Key words: biological fluid dynamics, flow–structure interactions, propulsion

†Email address for correspondence: jaywant@mecheng.iisc.ernet.in
‡Present address: Engineering Mechanics Unit, Jawaharlal Nehru Centre for Advanced Scientific Research, Bangalore 560064, India.

1. Introduction

Thrust generation by flapping foils has been extensively investigated in numerous studies (Triantafyllou, Triantafyllou & Yue 2000; Triantafyllou, Techet & Hover 2004, and references therein). Inspired by the observation that most thrust-generating appendages (wings and fins) of natural swimmers and flyers are flexible to varying degrees (Wootton 1999; Daniel & Combes 2002), some recent studies have looked at flapping flexible foils (Shyy, Berg & Ljungqvist 1999; Shyy *et al.* 2010). While most studies are with forward velocity/free-stream flow, very few explore the limit of zero free-stream velocity (e.g. Freymuth 1990; Gustafson, Leben & McArthur 1992; Wang 2000; Lai & Platzer 2001; Shinde & Arakeri 2013), and even fewer explore flexible foils with zero free-stream velocity (e.g. Heathcote, Martin & Gursul 2004; Heathcote & Gursul 2007; Eldredge, Toomey & Medina 2010). In this paper, we consider a case of pure pitching (rotary oscillations) of a flexible foil under zero free-stream condition, a case which has not been studied previously.

At high Strouhal numbers, it has been observed that the jet and correspondingly the thrust from a rigid flapping foil are deflected at some angle to the free-stream direction; Strouhal number, $St = fA/U_\infty$, where f is flapping frequency, A is trailing edge excursion and U_∞ is free-stream speed. Godoy-Diana, Aider & Wesfreid (2008) characterize the wake and show that a reverse Bénard–Kármán vortex jet inclined to the free stream is obtained for $St \gtrsim 0.4$. Other studies also report deflected jets at high St (e.g. Lewin & Haj-Hariri 2003; von Ellenrieder & Pothos 2008; Godoy-Diana *et al.* 2009; Cleaver, Wang & Gursul 2012). For $St \lesssim 0.4$, the jet is symmetric. Convection of vortices away from the place of shedding with appropriate spacing between them is central to the formation of a symmetric reverse Bénard–Kármán vortex street. When present, the free-stream convects the vortices after being shed and is a key reason to form a symmetric jet. Rearrangement of the terms in Strouhal number as $St = [A/U_\infty]/[1/f]$ reveals that St is the ratio of two time scales characterizing vortex convection and formation, respectively. At high St, after it is shed a vortex is not convected away fast enough to make space for a new one; successively shed vortices are closely spaced leading to dipole formation and jet inclination (Godoy-Diana *et al.* 2009). Analogous to this in case of three-dimensional flows, recently (Dewey, Carriou & Smits 2012) observed the formation of bifurcated jets when the vortex rings self-induce velocities enough to pull the rings away from the centreline of the flow field. For rigid as well as flexible heaving foils, Heathcote & Gursul (2007) find that the inclination angle of the jet reduces with decrease in St (i.e. increase in U_∞). For the limiting condition of St tending to infinity ($U_\infty = 0$), non-symmetric jets are observed for heaving and pitching rigid foils (Freymuth 1990; Gustafson *et al.* 1992; Lai & Platzer 2001); the jets meander across the centreline either quasiperiodically (Heathcote & Gursul 2007, for purely heaving motion), or continually and randomly (Shinde & Arakeri 2013, for purely pitching motion).

Marais *et al.* (2012) recently showed that chordwise flexibility increases separation between successively shed vortices and prevents jet inclination up to $St = 1.2$ compared with the value of $St \simeq 0.4$ for rigid foils. We consider the limiting condition of $St \to \infty$ ($U_\infty = 0$) and show that our chordwise flexible foil generates a coherent, unidirectional jet with the corresponding thrust aligned along the centreline, for a particular range of values of effective flexibility. The paper is organized as follows. Section 2 describes the experiments, and the non-dimensional numbers relevant to the flexible structure–fluid interaction problem presented in the paper. We also propose here a convenient non-dimensional stiffness parameter to characterize deformation of the flexible flap. In § 3, we describe the instantaneous and mean flow structure.

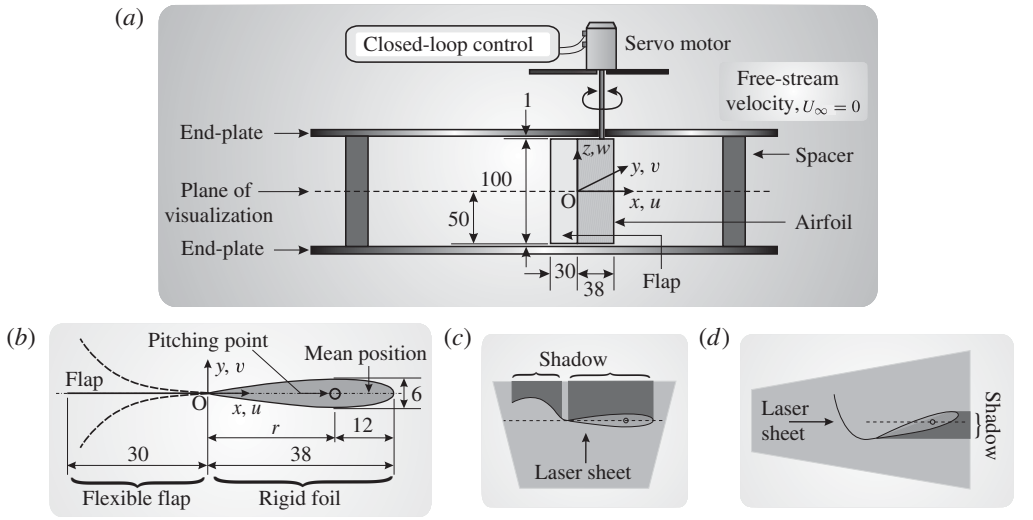

FIGURE 1. (*a*) Schematic of the experimental set-up. Spacers with circular cross-section are away from the foil so as to not affect the flow. Here x, y and z are the streamwise, transverse and spanwise directions, respectively; u, v and w are the corresponding velocity components. (*b*) Sectional view of the airfoil. Dimensions are in millimetres. (*c*) Optical arrangement for visualizations of the flow and the flap motion. Laser light is passed perpendicular to the airfoil chord axis. Flap is blackened except for a small portion near TE, which is transparent, so as to identify start of the flap–TE junction. (*d*) Optical arrangement for PIV. Laser light is passed from the TE end side along the airfoil chord axis in order to minimize the shadow cast by the airfoil; the flap is transparent for the PIV experiments that made it possible to get velocity data on both its sides.

In § 4, we show how flexibility suppresses jet deflection and meandering. Section 5 presents a parametric study. We also present values of thrust coefficients, which were obtained from the measured mean velocity fields. Section 6 presents the conclusions.

2. Experiments

Experiments are conducted in water in a glass tank (0.8 m × 0.8 m × 0.35 m). A servo motor sinusoidally oscillates the airfoil confined between two end-plates (figure 1*a*). The motor (30 W AC Panasonic A series RAMA3AZA1E) is driven by a Panasonic digital AC servo drive (MSDA3A3A1A, Type 1), and is controlled by Galil Motion Control card DMC 1425. The rigid airfoil has an NACA0015 profile with 38 mm chord c and 100 mm span (figure 1*b*). At the trailing edge, we firmly append along the rigid chord line a chordwise flexible transparent flap (30 mm chord c_f, 100 mm span s_f) made from 0.05 mm thick polythene sheet. The mass of the flap (= 0.15 g) is negligible compared with the fluid added mass (≈70 g, obtained by treating the flap as a plate moving normal to itself). The bending stiffness of the flap $EI = 3.15 \times 10^{-7}$ N m^2, where E is Young's modulus and I is moment of inertia of flap cross-section. In this paper, TE denotes trailing edge and FT denotes flap tip at its free end; quantities with overbar (e.g. $\overline{q}$) and star (q^*) indicate their time-mean and non-dimensional form (of q), respectively.

The pitching motion prescribed to the rigid foil is $\theta = \theta_{max} \sin(2\pi ft)$, where θ is instantaneous pitching angle, t is time, θ_{max} is amplitude and f is frequency of pitching.

We studied 12 cases: 3 amplitudes ($\pm10°$, $\pm15°$, $\pm20°$) and 4 frequencies (1, 2, 3, 4 Hz). We discuss in detail, in §§ 3 and 4, a representative case that falls nearly in the middle of the parameter range studied, namely $\theta_{max} = \pm15°$ and $f = 2$ Hz; we call this the 'standard case'. The distance of the nearest wall of the tank from the airfoil in the x direction is more than 10 chords and in the y direction more than 8 times $\Delta_{TE_{max}}$ (i.e. y-amplitude of TE deflection) for the largest-amplitude case ($\theta_{max} = \pm20°$).

The main diagnostics are visualizations and particle image velocimetry (PIV). Flow is recorded in a horizontal plane along the foil midspan (figure 1*a*) illuminated by a ∼1 mm thick laser sheet. We used two optical arrangements, one for visualization experiments (figure 1*c*) and another for PIV measurements (figure 1*d*). For visualization experiments, we used fluorescein disodium salt or polystyrene particles (75–100 μm), a continuous argon–ion laser (4 W, Spectra-Physics, Stabilite 2017) for illumination, and a Kodak Motion Corder Analyzer camera (SR-Ultra, 512 pixel × 480 pixel) to capture the flow images. The instantaneous velocity field is obtained using proVISION-XS™ PIV software from Integrated Design Tool (IDT), Inc. (Release 3.03). The flow was seeded with 30 μm hollow glass spheres (3M™ Scotchlite™ S Series, settling velocity 0.19 mm s^{-1}) that worked as tracers. We used 32 pixel × 32 pixel interrogation windows with 50 % overlap; the spatial resolution of the data is $0.064c$. For PIV, Nd:YAG dual pulsed laser (Quantel Big Sky Laser, ULTRA CFR, 120 mJ energy, pulse width 8 ns, pulse separation 3–19 ms) and SharpVISION™ camera (model-1400-DE, 1360 pixel × 1036 pixel, 70–300 mm ($f\# = 5.6$) macro zoom lens) were used. We varied the acquisition rate between 1 and 5 Hz. Overall error is estimated to be approximately 1 % of the instantaneous maximum streamwise velocity. Note that we do not resolve boundary layers around the foil and the flap. Further details on experiments are available in Shinde (2012).

2.1. *Non-dimensional numbers*

For a foil pitching in a free-stream flow (U_∞), in addition to the geometrical parameters of the foil, we have the following standard non-dimensional numbers: Reynolds number ($U_\infty c/\nu$, where ν is the kinematic viscosity of water), amplitude of pitching (θ_{max}), Strouhal number ($St = f\Delta_{TE_{max}}/U_\infty$), reduced frequency ($k = 2\pi fc/U_\infty$) and pitch-point location ($1 - r/c$) where r is the distance along the chord line of the pitching point from TE (see figure 1*b*).

For our case, free-stream velocity $U_\infty = 0$, thus both St, $k \to \infty$, and Reynolds number is zero. We define an alternate Reynolds number based on maximum velocity of TE ($V_{TE_{max}}$) as $Re = V_{TE_{max}} c/\nu$. Note that using $V_{TE_{max}}$ as velocity scale and $\Delta_{TE_{max}}$ or c as length scale, both k and St are either constants or reduce to θ_{max} (which is a parameter already listed); for more details, see the online supplementary material available at http://dx.doi.org/10.1017/jfm.2014.480.

Having a flexible flap leads to additional non-dimensional parameters. The geometrical parameters are normalized flap length (c_f/c) and normalized flap thickness (t_f/c). (Alternately, the flap length may be normalized by the y-amplitude of the TE deflection, i.e. $c_f/\Delta_{TE_{max}} = c_f/2\,r\,\sin(\theta_{max})$.) The mass ratio, which represents the ratio of flap inertia to fluid inertia is $\sim\rho_{flap} t_f/\rho\, c_f$, where ρ_{flap} is flap material density and ρ is fluid density.

To characterize the flexibility of the flap, we can define 'effective stiffness' EI^*. In the present fluid–flexible flap interaction problem, the deflection of the flap is determined by, in addition to the other parameters, the structural stiffness of the flap and the fluid forces acting on the flap. If we account for all of the forces acting

on the flap, the flap deflection can be obtained from the unsteady Euler–Bernoulli beam equation. We expect the fluid forces on the flap to scale as $\rho V_{TE_{max}}^2 s_f c_f/2$. Thus, treating the flap as a uniformly loaded cantilever beam, we get the FT deflection as $\delta_{FT} = w\, c_f^4/8EI$, where $w = \rho V_{TE_{max}}^2 s_f/2$ is load per unit length. We define the 'effective' stiffness parameter as $EI^* = c_f/\delta_{FT}$. Substituting for δ_{FT}, we get

$$EI^* = \frac{8\,EI}{\frac{1}{2}\,\rho\, V_{TE_{max}}^2\, s_f\, c_f^3}. \tag{2.1}$$

Similar definitions of effective stiffness for flexible surfaces have been used (Kang *et al.* 2011; Dewey *et al.* 2013; Shukla, Govardhan & Arakeri 2013), except that in these cases the pressure is based on the free-stream velocity. Equation (2.1) suggests that EI^* can be varied in various ways: by changing EI of the flap, flap length, f and θ_{max}. In our experiments, the variation in EI^* is obtained (over two orders in magnitude) by varying θ_{max} and f.

Treating the flap as a Euler–Bernoulli cantilever beam and considering mass of the flap as well as the added mass of the fluid, we can calculate the natural frequencies, f_{n1}, f_{n2}, etc. Another non-dimensional number related to flap stiffness can be defined in relation to the structural frequency of the flap, f/f_{n1}, where f_{n1} is the natural frequency corresponding to the first mode of flap bending. However, f/f_{n1} can be written in terms of already defined parameters, namely EI^*, c_f/c and θ_{max}.

A damping coefficient may be defined for the flap. For the flap material we are using, structural damping effects are expected to be much smaller than the damping due to fluid viscosity (Das, Govardhan & Arakeri 2013).

Thus, we have the following list of non-dimensional numbers relevant to the present experiments at $U_\infty = 0 : c_f/c$, $(1 - r/c)$, θ_{max}, mass ratio, Re and EI^*. In our experiments, c_f/c ratio is constant (=0.79), pitching point is fixed at the maximum thickness location of the rigid foil ($0.32\,c$ from the leading edge), and mass ratio is also fixed and is very small (=0.0017). Corresponding to the three θ_{max} values ($\pm 10°$, $\pm 15°$, $\pm 20°$) and the four flapping frequencies ($f = 1$, 2, 3, 4 Hz), the Reynolds number (Re) range is 1078–8625 and the EI^* range is between $\sim$0.04 and 2.30.

3. Flow structure

First, we discuss the flow corresponding to the standard case, $\theta_{max} = \pm 15°$ and $f =$ 2 Hz. How the flow changes as θ_{max} and f are varied is discussed in § 5.

The rigid foil pitching sinusoidally creates a spread out jet inclined to the centreline (figure 2*a*) that continually and randomly changes orientation. The flow from the rigid foil is discussed in detail by Shinde & Arakeri (2013). In dramatic contrast, for the same pitching conditions, attaching a chordwise flexible flap to the foil creates a coherent, undulating jet composed of vortices in a 'reverse Bénard–Kármán vortex street' aligned along the centreline (figure 2*b*). Thus, jet deflection and meandering are completely suppressed by chordwise flexibility. In § 5, we will show that such narrow, unidirectional jets are obtained only for flaps with EI^* values within a particular range.

Rotary oscillations of the foil generate complex flap motions. The flap undergoes very large deformations. It bends in the first mode (flap curvature is of one sign) during some phases and in the second mode (flap curvature is of two signs) during the other phases (figure 3*a*). The FT traces a distorted 'figure-of-eight' path about $x/c \approx -0.6$ (figure 3*b*). While, motion in the y direction is symmetric (about the

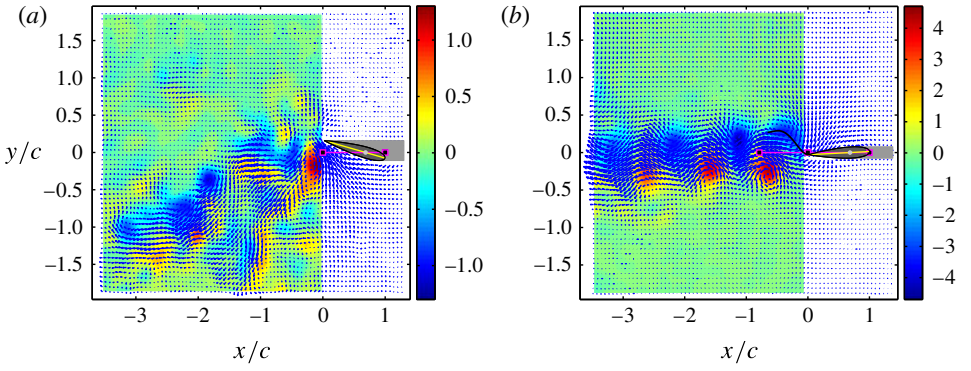

FIGURE 2. (*a*) Instantaneous flow field for the foil without flap; TE is moving up ($\theta_{max} = \pm 15°$, $f = 2$ Hz, $Re = 3234$). Vectors show velocity and contours show the normalized spanwise vorticity ($\omega_z^* = \omega_z/(V_{TE_{max}}/\Delta_{TE_{max}})$). Negative is clockwise vorticity and *vice-versa*. The flow is inclined downwards and the vortex positions do not show any order. (*b*) Same as (*a*) for the foil with flexible flap; at this instant FT is moving up and TE is moving down. In contrast to the flow in (*a*), the addition of the flexible flap produces a strong jet aligned along the centreline with vortices arranged in reverse Bénard–Kármán vortex street configuration.

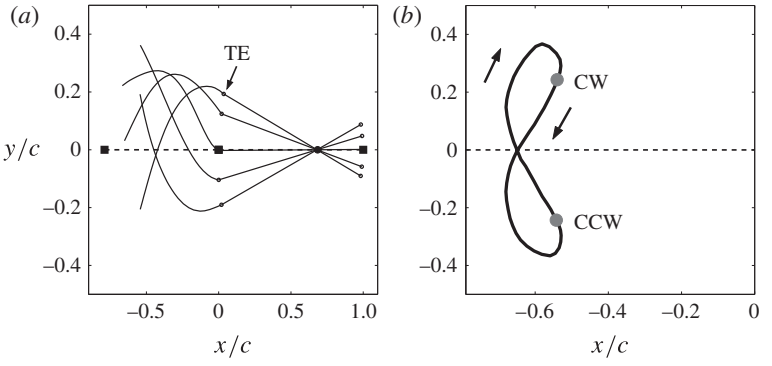

FIGURE 3. Details of flap motion corresponding to the flow shown in figure 2(*b*). (*a*) Flap profiles and airfoil chord positions at five phases over a half-cycle as the TE moves down. The broken line indicates the undeflected flexible flap if it were stretched along the centreline. (*b*) The FT locus over a cycle. Arrows indicate direction of FT motion. Grey dots show FT position when vortex is shed (CCW, counterclockwise; CW, clockwise).

mean position), it is not so in the x direction. The amplitude of FT deflection in the y direction is rather large compared with that in the x direction; the former is about twice and the latter is about half of the y amplitude of the TE deflection. There exists a phase difference between the TE and FT motion: FT trails TE by 137° in the y direction. Figure 3(*a*) clearly shows that the flap motion is like a travelling wave starting from TE with amplitude increasing in the downstream direction (see supplementary movie). There is a strong coupled interaction between the flow and the flap: flap motion is responsible for the creation of flow, and in turn, the flow affects the flap motion. Detailed discussion of the physics of flow generation is reported in Shinde (2012). In brief, the flow generation takes place due to the coordinated pushing

action of the foil and the flexible flap; they draw in the ambient fluid from the front and largely from the sides, and accelerate it downstream to form the coherent jet (see figure 2*b*).

Figure 4 shows the long time mean flow data for both the foils, with and without the flexible flap. It is evident from the velocity vector fields and the isovelocity contour plots that the foil without a flap produces a weak, inclined mean jet (figure 4*a*,*c*), whereas that with the flexible flap generates a strong, narrow jet aligned along the centreline (figure 4*b*,*d*). This can also be seen in figure 4(*e*,*f*) which show the profiles of mean velocity magnitude for the two foils. Figure 4(*b*) shows that the fluid in the vicinity of flexible flap region is pulled towards and by the flexible flap, and is pushed downstream as a narrow jet. Mean streamwise velocity profiles for the foil with flexible flap in figure 4(*g*) show near-Gaussian variation as in standard two-dimensional jets. The jet is confined mostly within a narrow region $y/c \approx \pm 0.5$ around the centreline. For the case with $\theta_{max} = \pm 15^{\circ}$ and $f = 2$ Hz, the maximum jet velocity is 136 mm s^{-1} ($\overline{u}_{max}/V_{TE_{max}} = 1.59$). The corresponding Reynolds number based on the maximum jet velocity and the jet width at this velocity location ($x/c = -1.61$) is 2028.

Note that a rigid flap attached to the airfoil would produce essentially the same flow as that of the foil without the flap; only the scale (due to increased chord length) will be changed. In other words, a foil with a rigid flap is expected to produce a weak, divergent jet as in figure 2(*a*). Our aim is to study how the jet meandering, which is found in the case of rigid foil, is eliminated, even in the absence of a free-stream flow, by the addition of a flexible flap.

4. Near-wake vortex dynamics and role of flexibility

In this section, we discuss the mechanisms by which a flexible flap suppresses meandering and produces a coherent, aligned jet. Both the foils, with and without the flexible flap, shed a pair of large counter-rotating vortices per cycle, but a coherent jet is observed only in the former case. Everything else being the same, this stark difference in the flows is intricately linked to the action of the flexible flap. We identify two physical mechanisms by which meandering is overcome to produce a unidirectional jet: shedding of the vortex at the appropriate spatial location and at an appropriate phase in the cycle, and convection of the vortex after it is shed.

4.1. *Appropriate vortex shedding*

Godoy-Diana *et al.* (2009) show that a pitching rigid foil produces an asymmetric or deflected jet above a critical *St* due to formation of vortex dipoles from two successively shed counter-rotating vortices. One of the factors that determines dipole formation is the inter-vortex spacing. Recently, Marais *et al.* (2012) found that foil flexibility increases vortex spacing, prevents dipole formation, and essentially, inhibits jet deflection at higher *St* (in effect lower free-stream speed) compared with the rigid foil. In the present experiments, jet deflection is completely suppressed in the limit of $St \to \infty$, zero free-stream velocity.

In our case also, the flexible flap increases the separation between successively shed vortices compared with the rigid foil case. Figure 5 clearly shows that the addition of the flexible flap increases the spacing by approximately 2.3 times, whereas chord length increase is 79 %. We observe that a new vortex is shed when the FT is closest to the TE in the x direction and when it is moving towards the centreline (see figure 3*b*). Due to the bending action of the flexible flap, the newly born vortex that

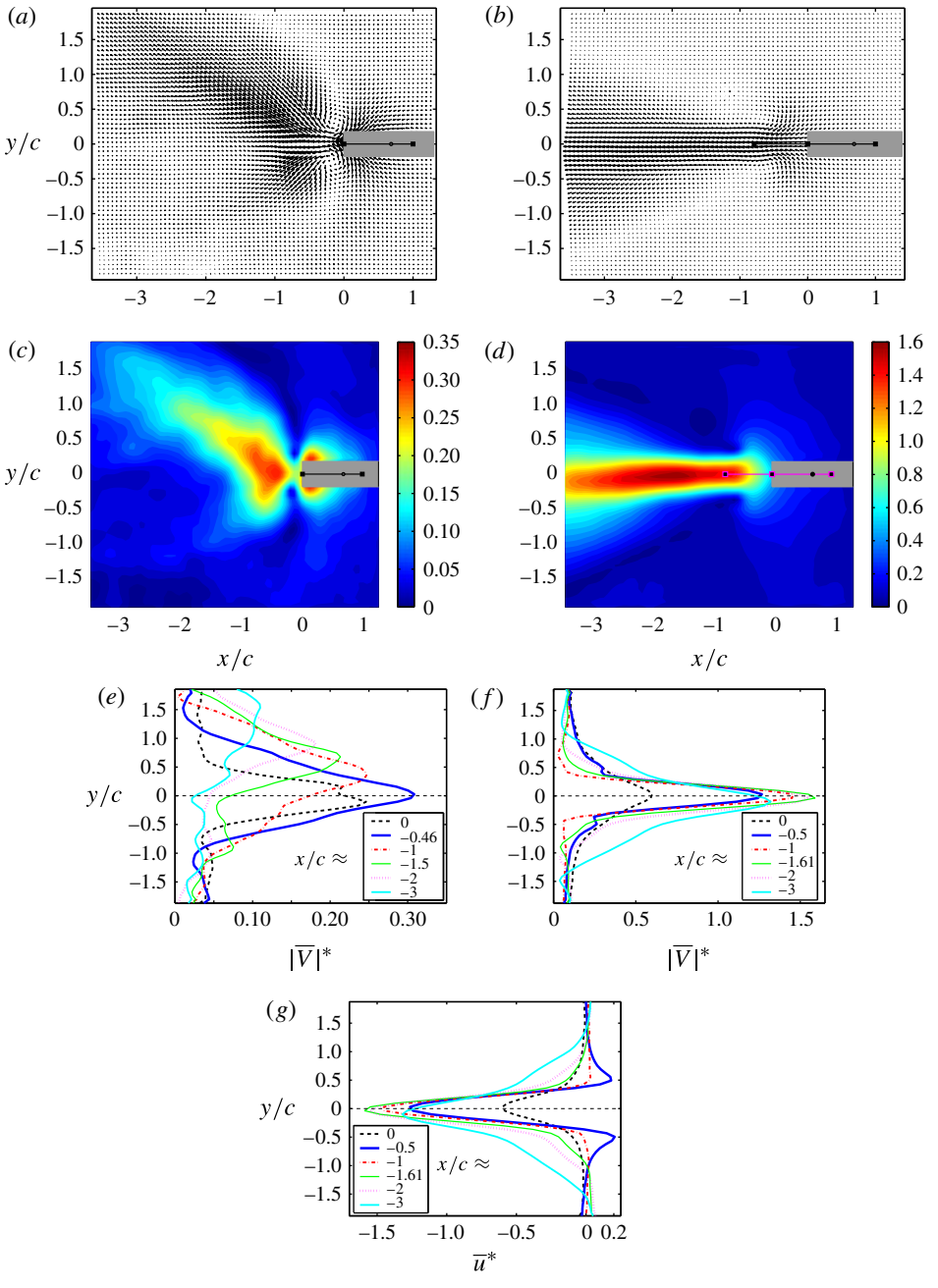

FIGURE 4. Mean velocity data for the cases shown in figure 2. Flow velocity is normalized by $V_{TE_{max}}$. (*a*,*c*,*e*) are for the pitching foil without flap; averaging is over 130 cycles. (*b*,*d*,*f*,*g*) are for the foil with the flexible flap; averaging is over 220 cycles. (*a*,*b*) Velocity vectors for the two foils. (*c*,*d*) Isocontours of velocity magnitude. The grey rectangular patch in (*a*,*b*,*c*,*d*) is the region where PIV data is absent because of the presence of foil and its shadow. The profiles of velocity magnitude (*e*,*f*) and streamwise velocity (*g*) at several downstream x locations.

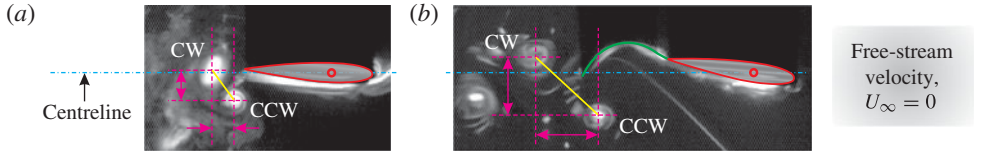

FIGURE 5. (Colour online) (*a*) Dye visualization for the foil without flap; the TE is moving up. (*b*) Visualization for the foil with flexible flap; the FT is moving up and the TE is moving down. In both cases, dye is released continuously from ports on both surfaces of the foil at the maximum thickness location. Appending the flexible flap to the foil increases the spacing between successively shed counter-rotating vortices.

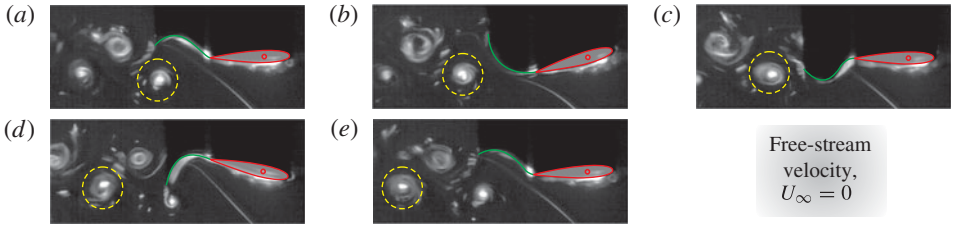

FIGURE 6. (Colour online) Dye images at several phases over one cycle. The counterclockwise vortex (enclosed by a dashed circle) convects about a chord downstream during this time. In (*a*,*c*,*e*) the TE is near the mean position. In (*a*,*e*) the TE is moving down and in (*c*) it is moving up. In (*b*) the TE is near the bottom-extreme position and in (*d*) near the top-extreme position.

is cast off from FT is shed slightly upstream compared with if the flap were rigid as can be seen in figure 5(*b*). Deformation of the flexible flap increases the overall separation between a just-shed vortex and the one shed previously, thus preventing dipole formation.

4.2. *Vortex convection*

Once the vortex is shed, it has to be convected away. In the absence of a free-stream, however, vortex convection has to be necessarily induced by the flap motion. This is in fact the second important function of the flexible flap. Figure 6 demonstrates the convection of a newly shed vortex in one oscillation cycle period.

To see the initial development of the vortex street, we track the positions of a vortex from the time just after it is shed until it finally becomes part of the reverse Bénard–Kármán vortex street, which is aligned along the centreline. Following Godoy-Diana *et al.* (2009) and Marais *et al.* (2012), we identify the vortex position by its centre, i.e. local peak vorticity location, $[x_{vort}(t), y_{vort}(t)] = [x(t), y(t)]|_{\omega_z(t)_{peak}}$. We track the paths of two successively shed counter-rotating vortices ('CCW vortex' and 'CW vortex') over one time period (τ). Figure 7 shows the x position (figure 7*a*) and the y position (figure 7*b*) as functions of time of these two vortices. We take $t/\tau = 0$ to be just after the CCW vortex is shed; the CW vortex is shed in the previous half-cycle and is at $x/c = -0.9$, $y/c = 0.17$ at this time. The CW vortex is part of the vortex street and is moving with constant x velocity of approximately 74 mm s^{-1}, i.e. approximately $1\,c/\tau$, parallel to the centreline at $y/c = 0.17$. (For the foil without the flap, it is not possible to track the vortices in a similar manner as they smear out rapidly (figure 5*a*) and lose identity within a short distance.)

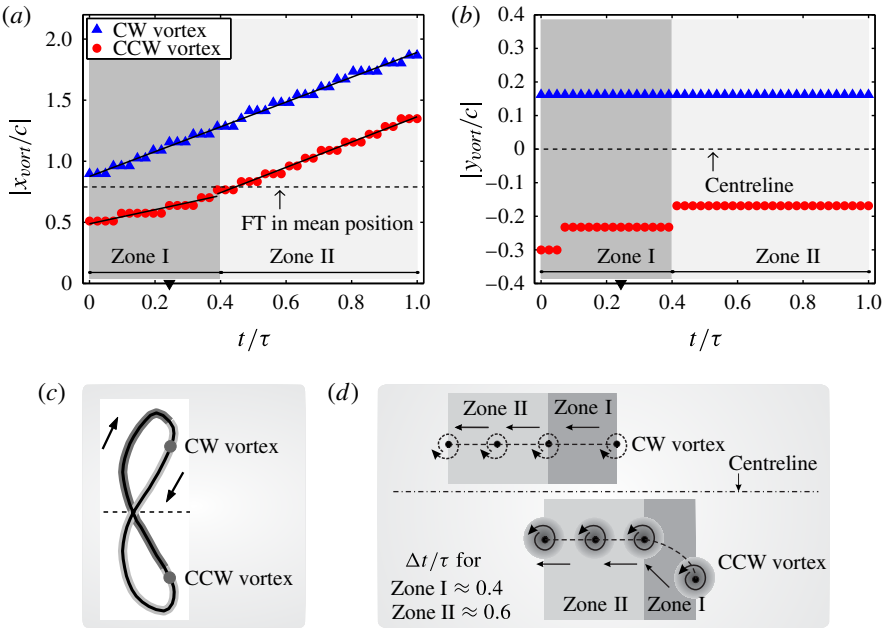

FIGURE 7. (Colour online) (*a*,*b*) Position versus time over one time period for two consecutively shed vortices (CCW, counterclockwise; CW, clockwise): (*a*) x positions and (*b*) y positions. Here $t/\tau = 0$ corresponds to the time just after CCW vortex is shed; τ is cycle period. The stepwise change in the position data corresponds to the resolution of $\pm 0.032\,c$. In (*a*) the black lines are fits to position data. Here ▼ on abscissa is the time when the TE is at the mean position and is moving down. (*c*) The FT locus; the dark line corresponds to time zone I and the light line to zone II (see the text). The grey dots indicate FT locations when the vortices are shed. Arrows indicate the direction of FT motion. (*d*) Schematic of the trajectories of the two vortices. During zone I, the CCW vortex shed away from the centreline moves towards its eventual position in zone II.

To see how the CCW vortex merges into the vortex street and continues to move along the centreline, we divide the cycle for convenience into two time zones namely zone I ($t/\tau \approx 0$–0.4) and zone II ($t/\tau \approx 0.4$–1.0). Figure 7(*c*) shows the motions of the FT corresponding to the two time zones.

The CCW vortex is shed at around $|x/c| = 0.5$ (figure 7*a*), and at $y/c = -0.3$, away from its eventual location of $y/c = -0.17$ (figure 7*b*); as discussed above, this higher initial separation between the vortices prevents dipole formation and, thus, jet deflection. The CCW vortex moves towards the centreline until it reaches its steady y position at the end of zone I (see figure 7*b*). During zone I, figure 7(*a*) shows that CCW vortex speed is lower at approximately 0.63 of its final speed. In zone II, the steady staggered configuration is reached and the two vortices travel only in the x direction with the same speed (figure 7*a*,*b*) forming part of the vortex street. After being shed, a vortex travels a distance of approximately $0.26\,c$ and takes about t/τ of 0.4 to reach its final steady speed. Figure 7(*d*) shows schematically the motion of the vortices in zones I and II.

Once a vortex is shed, its subsequent motion is determined by three important agencies: free-stream flow (if present), induced motion of downstream vortices and flow created by the foil itself. If the vortex is not convected away either by the free-stream flow or as in our case by the flap action, the vortex would destructively

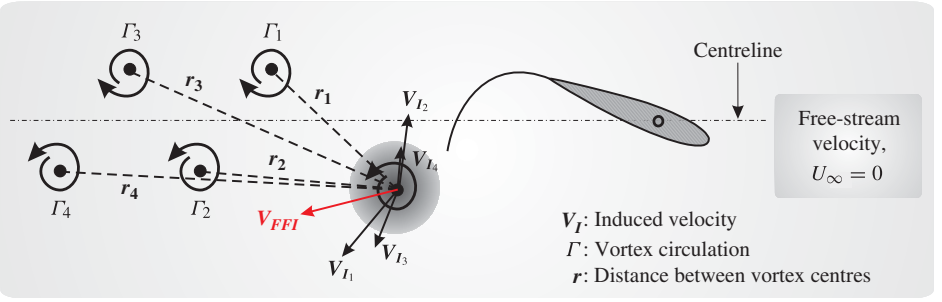

FIGURE 8. (Colour online) For the flow caused by pitching foil with the flexible flap, a vortex which is just shed (shown enclosed in a grey circle) has induced velocity contributions (e.g. $\boldsymbol{V}_{I_1}$, $\boldsymbol{V}_{I_2}$, etc.) from the vortices which are present to its left. Here $\boldsymbol{V}_{FFI}$ is the velocity due to the flow induced by the flexible flap and airfoil motion.

interact with the vortex which will be shed subsequently. Thus, generation of an undeflected jet in zero free-stream condition is due to the twin actions by the flap: one, appropriate location and phase of vortex shedding; and two, convection of the shed vortex to make space for the new one. The online supplementary movie demonstrates how the flexible flap performs these actions.

One useful way to think about the action of the flexible flap is as shown in figure 8. The action of the flow created by the airfoil and flap motion can perhaps be best explained with reference to this figure. To the left of a vortex that is just shed, we have an array of vortices shed previously from the FT. The vortices move to the left with a constant velocity. The motion of each vortex is due to the velocities induced by the rest of the vortices in the wake and due to the flow induced by the motion of the foil and the flexible flap. Treating wake vortices as point vortices, vortex convection velocity can be written as

$$\boldsymbol{V}_{vortex}(x, y, t) = \underbrace{\boldsymbol{V}_{FFI}(x, y, t)}_{\text{Effect of flow due to foil and flexible flap}} + \underbrace{\sum_{k=1}^{n} \boldsymbol{V}_{I_k}(x, y, t)}_{\text{Effect of wake vortices}}. \tag{4.1}$$

The first term on the right-hand side in (4.1), $\boldsymbol{V}_{FFI}$, represents the velocity induced on the vortex under consideration due to the flow created by the foil and the flexible flap motions. Note that, as discussed briefly in § 3, in the absence of free-stream flow, the entire flow creation takes place by the motion of the foil and the flexible flap. Of course, this induced velocity ($\boldsymbol{V}_{FFI}$) can be modelled using potential flow, for example, with a panel method and with an appropriate Kutta condition. To get the flap motion itself, the flap has to be modelled, for example, as an Euler–Bernoulli beam equation and the full fluid–flap interaction problem has to be solved. The second term on the right-hand side in (4.1) is the induced velocity from all of the vortices in the wake; $\boldsymbol{V}_{Ik} = \Gamma_k/2\pi\boldsymbol{r}_k$ is the velocity induced on the vortex under consideration by k^{th} vortex with circulation Γ_k situated at a distance of $\boldsymbol{r}_k$ from it and n is a sufficiently large number of vortices in the wake. If free-stream flow is present, it would provide one additional component in (4.1) to the vortex velocity.

The velocity fields obtained from PIV measurements give a good idea on the nature of the flow created by the flap and foil. Figure 9(*a*,*b*) show the flow and vorticity fields just after the CCW vortex is shed. It is important to realize here that the CCW

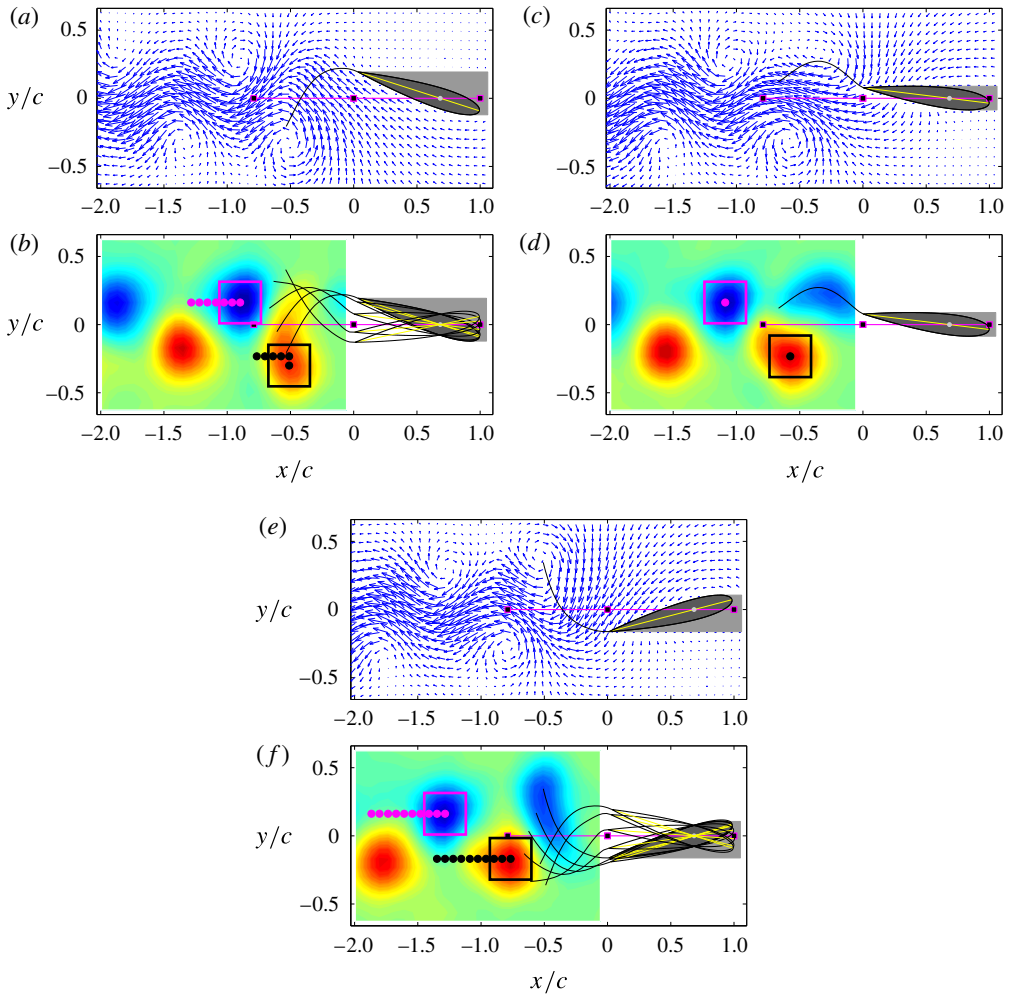

FIGURE 9. (Colour online) Velocity (*a*,*c*,*e*) and vorticity (*b*,*d*,*f*) fields at $t/\tau = 0$ (*a*,*b*), 0.2 (*c*,*d*) and 0.42 (*e*,*f*). The positions (shown as dots) of two vortices (enclosed in squares) are tracked over the two time zones. (*b*) shows the vortex positions and flap profiles for a few phases in zone I and (*f*) the vortex positions and flap profiles in zone II.

vortex is shed almost at the correct location; and in addition, the flow around the flap is such that it provides the convective motion to the vortex in the downstream direction. Figure 9(*c*) shows, as an example, the flow field at the middle of zone I ($t/\tau = 0.2$), due to flap and foil motions which are responsible for this convection. At $t/\tau = 0.4$ and beginning of zone II, the new half-cycle is about to begin and a new CW vortex is being formed at the FT (see figure 9*e*,*f*). Figure 9(*b*,*f*) depict the flap profiles and the motions of the two vortices during the two zones. Note that in zone I and large fraction of zone II, the FT and TE move in opposite directions (figure 9*b*,*f*).

5. Parametric study and thrust estimation

In the previous section, we showed the crucial role of flexibility of the attached flap in generating a coherent, unidirectional jet and, hence, thrust. Next we look at in what

θ_{max}	f (Hz)	$\Delta_{TE_{max}}$ (mm)	$\Delta^*_{FT-x_{max}}$	$\Delta^*_{FT-y_{max}}$	$V_{TE_{max}}$ (mm s^{-1})	$V^*_{FT-x_{max}}$	$V^*_{FT-y_{max}}$	Φ_y (deg.)	EI^*	Re
±10°	1	9.0	0.14	0.84	28.5	0.54	1.67	120	2.30	1078
	2	9.0	0.19	1.10	57.0	1.03	2.24	156	0.57	2156
	3	9.0	0.20	1.27	85.5	1.06	2.35	185	0.26	3234
	4	9.0	0.17	1.13	114.1	0.93	2.43	197	0.14	4312
±15°	1	13.5	0.13	0.82	42.8	0.66	1.57	109	1.02	1617
	2	13.5	0.20	0.96	85.5	0.92	1.77	137	0.26	3234
	3	13.5	0.24	0.96	128.3	1.23	1.76	163	0.11	4851
	4	13.5	0.34	1.01	171.1	1.63	2.03	162	0.06	6468
±20°	1	17.8	0.13	0.78	57.0	0.62	1.40	93	0.57	2156
	2	17.8	0.21	0.89	114.1	0.94	1.66	120	0.14	4312
	3	17.8	0.30	0.91	171.1	1.60	1.67	130	0.06	6468
	4	17.8	0.45	0.91	228.1	2.58	1.85	122	0.04	8625

TABLE 1. Deflections and velocities of TE and FT, EI^* values and Reynolds number for the 12 cases. Here Φ_y is the phase difference in the y direction motion between TE and FT; TE leads FT in all cases. Here $\Delta^*_{FT-x_{max}}$ and $\Delta^*_{FT-y_{max}}$ are respectively the x and y amplitudes of the FT deflection, which are non-dimensionalized by the calculated y-amplitude of FT deflection if the flap was rigid. Here $V^*_{FT-x_{max}}$ and $V^*_{FT-y_{max}}$ are the maximum velocities of FT respectively in the x and y directions non-dimensionalized by the maximum TE velocity $V_{TE_{max}}$.

way the flap deflections and the nature of the jet change with flapping amplitude and frequency. We observed that changing the values of these parameters greatly changed the flap deflection profiles. Below we will show that the non-dimensional stiffness EI^* (defined in § 2.1) is a key parameter for the present fluid–structure interaction which dictates the flow structure and determines whether we get a coherent jet or not.

In table 1, we list the different parameter values related to TE and FT motions, and the EI^* and Re values for each of the 12 cases.

5.1. *Flap kinematics*

We observed that in all of the 12 cases studied, the FT executes 'figure-of-eight' motion with flap geometry becoming in general more distorted with decrease in EI^* (with increase in flapping amplitude and frequency). Figure 10 shows the variations in flap deformation and its motion for four representative cases. As EI^* reduces, the flap deformation as well as the distortion of the FT 'figure-of-eight' motion increase, indicating that the flap becomes effectively more flexible. For the cases with very low EI^* values, the flap bends in third mode too during some phases (see, e.g. figure 10*d*). Further, as the EI^* reduces, the location about which the FT traces the 'figure-eight' locus moves towards the TE and the FT deflection in the x direction increases while that in the y direction shows much less variation.

The normalized maximum FT deflection in the y direction ($\Delta^*_{FT-y_{max}}$) versus frequency for the three θ_{max} values is shown in figure 11. The FT deflection is normalized by the tip deflection of a flap if it were rigid ($\Delta_{FT-y-Rigid_{max}}$). In the case of $\theta_{max} = \pm 15°$ and ±20°, no peaks are observed and the normalized y-deflection amplitude of FT is nearly constant, ∼1. For three of the four cases with $\theta_{max} = \pm 10°$, the $\Delta^*_{FT-y_{max}}$ values are observed to be above 1, and the maximum is at $f = 3$ Hz. Using the Euler–Bernoulli beam equation and treating the flap as a cantilever beam,

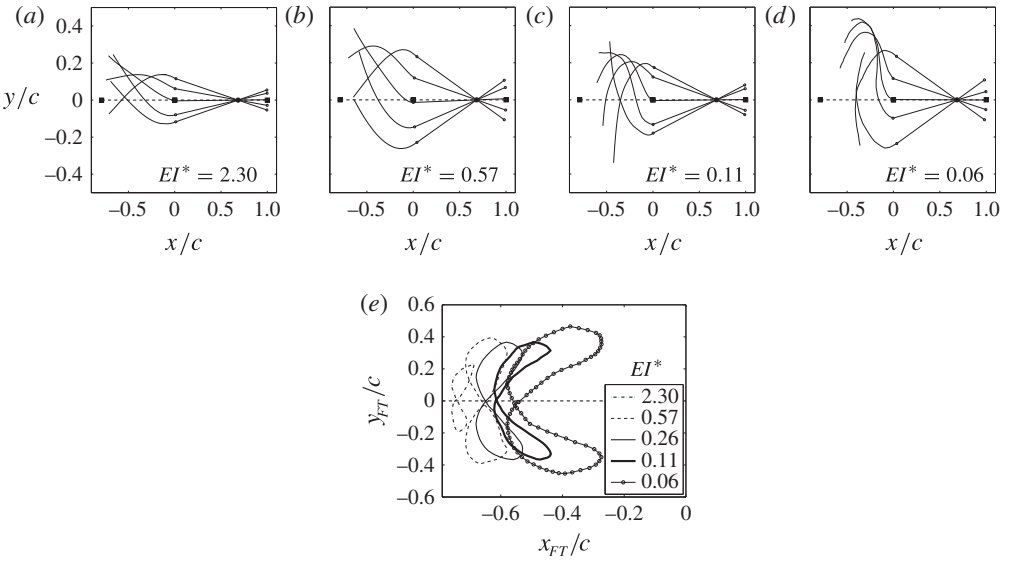

FIGURE 10. Flap profiles at five phases, as the TE moves down, for (*a*) $\theta_{max} = \pm 10°, f =$ 1 Hz, (*b*) $\pm 20°$, 1 Hz, (*c*) $\pm 15°$, 3 Hz, (*d*) $\pm 20°$, 3 Hz. (*e*) FT loci for cases in (*a–d*) and in figure 2(*b*). With reduction in EI^*, flap bending increases and 'figure-eight' becomes increasingly distorted; for $EI^* = 0.06$, the flap bends in third mode (*d*).

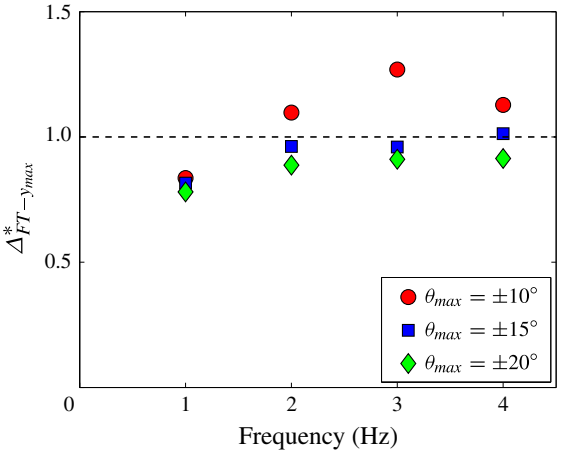

FIGURE 11. (Colour online) The y amplitude of FT deflection non-dimensionalized by the y amplitude of FT deflection if the flap was rigid, i.e. $\Delta_{FT-y-\mathrm{Rigid}_{max}}$.

we obtain the natural frequency for the first mode $= 0.23$ Hz and for the second mode as 1.43 Hz. These values are obtained using an added mass value $= 70$ g distributed uniformly on the flap. However, we cannot comment, whether the maximum at $f = 3$ Hz is an indication of resonance. To do a systematic study of resonance, experiments with a large number of flaps with different lengths and stiffnesses are required, which will be considered in the future.

Figure 12 shows the data for FT deflection in the y and x directions versus EI^*. Figure 12(*a*) shows that there is no clear trend for $\Delta^*_{FT-y_{max}}$, but the deflections lie in a narrow range between 0.78 and 1.27, when EI^* varies over nearly two

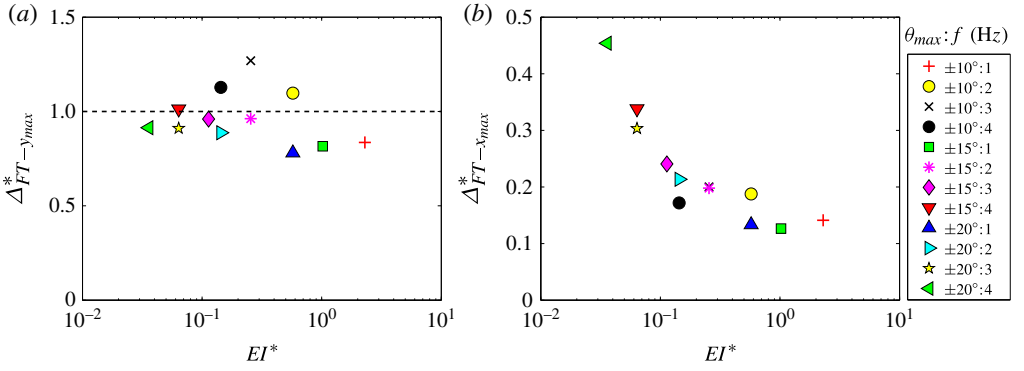

FIGURE 12. (Colour online) FT kinematic data for all 12 cases: (*a*) y amplitude; (*b*) x amplitude. FT deflection amplitude non-dimensionalized by the y amplitude of FT deflection if the flap was rigid, i.e. $\Delta_{FT-y-\mathrm{Rigid}_{max}}$.

orders of magnitude. However, the data for the maximum FT deflection in the x direction ($\Delta^*_{FT-x_{max}}$) plotted versus EI^* show a much larger variation (0.13–0.45) and when plotted against EI^* seem to lie on a single curve as seen in figure 12(*b*). The x direction FT deflections increase rapidly with decreasing EI^*, consistent with increasing distortion of the FT locus with decreasing effective stiffness. The larger variations in FT deflections in the x direction compared with those in the y direction are reflected in the FT velocity variations in the two directions (see table 1): variation in $V^*_{FT-x_{max}}$ is approximately 3 times the variation in $V^*_{FT-y_{max}}$. The maximum in FT velocities in the two directions are approximately 2.5 times the TE velocity $V_{TE_{max}}$.

5.2. *Jet structure*

The changes in flap deformation dictate the flow structure. In all cases studied, despite the large variations in flap motion, only two large counter-rotating vortices are shed every cycle; in all cases, these are shed when the FT moves towards the centreline in the y direction and away from the TE in the x direction. However, a coherent jet is not obtained in all cases and the deformation characteristics of the flap do influence the nature of the flow. Figure 13 shows the flow field for the same four cases shown in figure 10. For the highest EI^*, the flap is effectively stiff and the jet starts meandering after travelling on the centreline for some distance (about two chords, see figure 13*a*). This is similar to the rigid foil case ($EI^* \to \infty$), except that there the meandering starts almost immediately at the TE (figure 2*a*). When the flap is effectively highly flexible (large θ_{max} and f, small EI^*), the jet moving along the centreline spreads rapidly beyond $x/c \approx -2$ (figure 13*d*). It is only within a particular effective stiffness range of EI^*, ∼0.1–1, that deformations are optimal for generating a coherent, orderly jet aligned along the centreline (figure 13*b*,*c*); EI^* for the standard case is 0.26 (figure 2*b*).

To calculate the spread of the jet, we define the local jet width (JW) as the distance between the maximum and minimum mean vorticity locations. We measure the jet spread as JW at $x/c = -2.5$ normalized by JW at the 'start' of the jet. Figure 14 shows that there is very little change in JW for the moderately stiff flaps ($EI^* \sim$ 0.1–1); on either side of this range, $EI^* \lesssim 0.1$ and $EI^* \gtrsim 1$, the JW increases rapidly, corresponding respectively to spreading and meandering jets.

For the relatively stiff case ($EI^* = 2.3$), the initial vortex spacing is smaller than the coherent jet cases which perhaps leads to the meandering jet. We do not have an

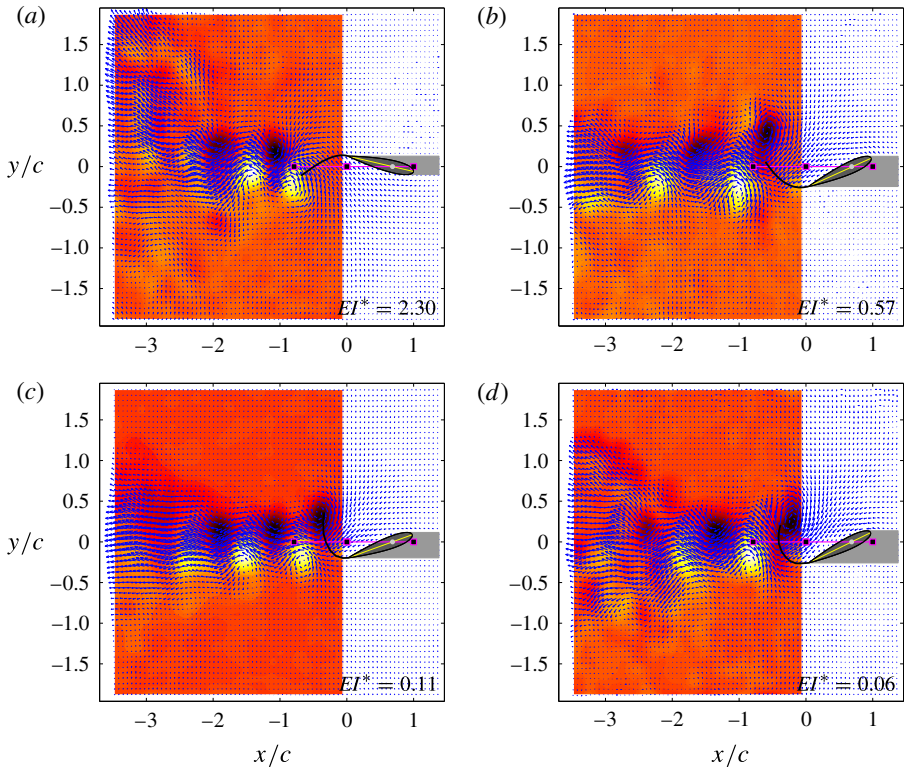

FIGURE 13. (Colour online) Velocity–vorticity snapshots for (*a*) $\theta_{max} = \pm 10°$, $f = 1$ Hz, (*b*) $\pm 20°$, 1 Hz, (*c*) $\pm 15°$, 3 Hz and (*d*) $\pm 20°$, 3 Hz. For the $EI^* = 2.30$ case, the jet meanders (*a*); for the $EI^* = 0.06$ case it rapidly spreads out beyond $x/c \simeq -2$ (*d*). For the other two cases, $EI^* = 0.11$ and 0.57, narrow, aligned jets are obtained (*b*,*c*).

explanation for the sudden jet widening when the flap is highly flexible ($EI^* = 0.06$); although in this case we do observe that the vortex is shed closer to the leading edge because of the very large flap deformation. For the moderately stiff flaps, it appears that the shedding location of the vortex and its subsequent motion are just right for producing a coherent, non-deflected jet.

This study shows that EI^* is an important non-dimensional number in capturing the physics of the fluid–flexible surface interaction. In a single parameter, EI^* seems to capture the coupling between the fluid and elastic forces on the flap, which determine the flap deformation profiles and in turn the final flow. We have varied EI^* only by changing f and θ_{max}, but we plan to conduct experiments with different flap lengths and different EIs to establish whether EI^* uniquely determines the flow structure. We will know in particular if the effect of change in length of the flap is captured by EI^*. However, we may expect the length effect not to be fully captured for very long and very short flaps. We believe, however, that this parameter will have more general application wherever flexible wings are found, as in birds, insects and fish.

5.3. *Thrust estimation*

The mean thrust generated by a flapping foil can be estimated from the wake flow measurements using the standard integral momentum balance for a control

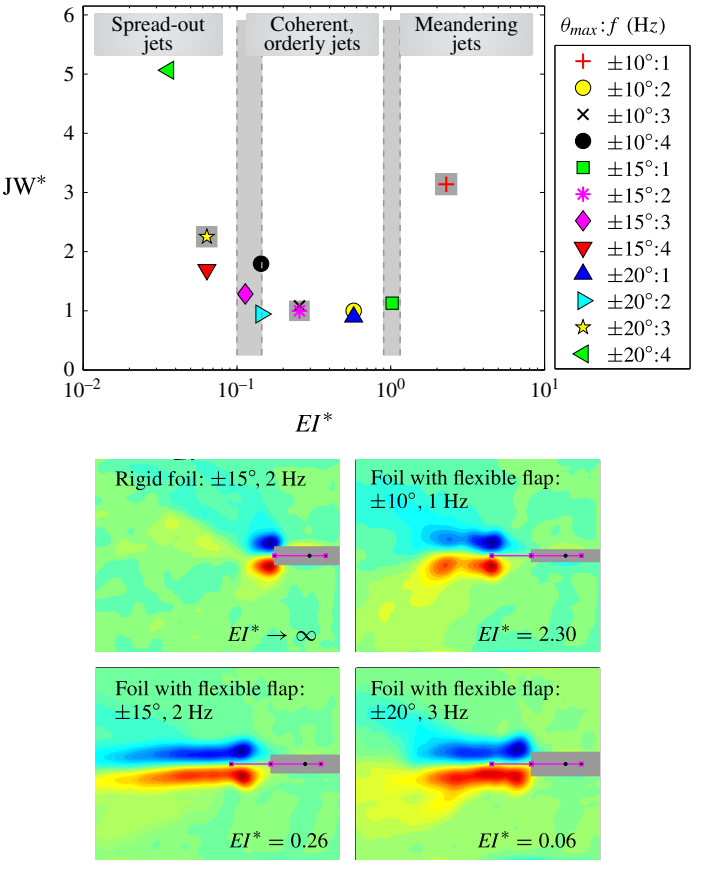

FIGURE 14. (Colour online) Variation of the normalized jet width (JW*) with EI^*. Here JW* = JW2/JW1, where JW2 is jet width (defined in the text) at $x/c = -2.5$, and JW1 is jet width at the location where mean vorticity magnitude is maximum (usually in the flap region). Large widening of the jet is observed for $EI^* \lesssim 0.1$ and $EI^* \gtrsim 1$. Images given below the *JW*–EI** plot show mean vorticity plots for cases representative of the three flow regimes; these cases are highlighted by grey squares in the JW*–EI^* plot. Also shown is the case for the foil without flap ($EI^* \to \infty$).

volume enclosing the foil (Anderson *et al.* 1998; Godoy-Diana *et al.* 2008; Bohl & Koochesfahani 2009). The streamwise momentum flux at a sufficiently downstream location is essentially equal to the mean thrust. Bohl & Koochesfahani (2009) showed that in the case of strongly fluctuating velocity fields (e.g. those due to oscillating foils), contributions from streamwise velocity fluctuations and pressure calculated from the transverse velocity fluctuations (v') can be non-negligible. Including the corrections due to streamwise and transverse velocity fluctuations, the expression for mean thrust coefficient is

$$\overline{C_T} = \left. \frac{\rho \int_{-\infty}^{\infty} \overline{u^2}\,\mathrm{d}y - \rho \int_{-\infty}^{\infty} \overline{v'^2}\,\mathrm{d}y}{\frac{1}{2}\rho V_{TE_{max}}^2 c} \right|_{x/c=-2.5}. \tag{5.1}$$

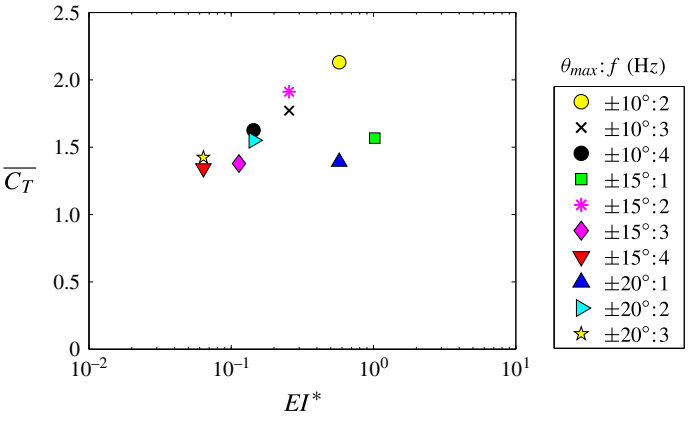

FIGURE 15. (Colour online) Mean thrust coefficient for all except the two extreme cases, namely $EI^* = 2.30$, $\theta_{max} = \pm 10°$, $f = 1$ Hz and 0.04, $\pm 20°$, 4 Hz.

Inclusion of these corrections, mainly the fluid pressure term, essentially addresses the concerns raised by Dabiri (2005) in estimating the thrust from the mean velocity field data. Note, $\overline{C_T}$ is defined based on maximum velocity of the TE ($V_{TE_{max}}$) instead of the free-stream speed, which in our case is zero. We calculate the momentum flux at $x/c = -2.5$ where the jet is well established.

The mean thrust coefficients obtained using (5.1) for the foil with the flexible flap are plotted against EI^* in figure 15; it is 1.91 for the standard case ($\theta_{max} = \pm 15°$ and $f = 2$ Hz). Thrust is calculated for the cases for which a coherent, unidirectional jet along the centreline is obtained. Thrust is not calculated for the two extreme cases, namely $EI^* = 2.30$, $\theta_{max} = \pm 10°$, $f = 1$ Hz for which the jet meanders and $EI^* = 0.04$, $\theta_{max} = \pm 20°$, $f = 4$ Hz for which the jet spreads. Thrust coefficients for different cases with the same EI^* are nearly the same for the lower values of EI^*. However, the two cases for $EI^* = 0.57$, corresponding to $\theta_{max} = \pm 10°$, $f = 2$ Hz and $\theta_{max} = \pm 20°$, $f = 1$ Hz show very different $\overline{C_T}$ values. We do not know the reason for this difference, but we do observe that in the case of $\theta_{max} = \pm 20°$, $f = 1$ Hz, the phase difference between the TE and FT displacements in the y direction is the lowest (=93°) among all cases (see table 1). In general, the non-dimensional thrust increases with increase in EI^* until about $EI^* = 0.5$. For $EI^* \gtrsim 1$, when the jets meander, we would expect thrust to decrease, the values of which can only be obtained through direct force measurements. We plan to make direct measurements of the unsteady forces and torque which will clearly establish the relation between the generated thrust and EI^*. In addition, these measurements will be useful to optimize various parameter values such as flap length, flap stiffness and pitching-point position.

6. Conclusions

The present experiments in the limiting case of zero free-stream velocity ($St \to \infty$) show that a purely-pitching foil with a flexible flap, of appropriate stiffness, attached to it can generate a narrow jet, whose direction and thus its thrust are aligned along the centreline. This is in contrast to a rigid pitching foil which produces a weak and meandering jet (and thrust). Deformations of the flexible flap suppress meandering by increasing the initial spacing between successive vortices and by imposing a convective motion on the shed vortices even in the absence of free-stream velocity.

Our results are consistent with, but add to, those of Marais *et al.* (2012) where they show that flexibility increases the *St* (up to 1.2) at which non-deflected jets are obtained.

The extent of flap deformation or deflection is determined both by the structural stiffness of the flap and the fluid loading, in addition to the other parameters involved in the fluid–flexible structure interaction. We have used a non-dimensional 'effective stiffness', EI^*, which incorporates the structural stiffness of the flap and the fluid forces to characterize flap deflection. Our experiments, for EI^* variation over two orders of magnitude, show that coherent, unidirectional jets aligned along the centreline are generated for those cases when the flap is moderately stiff: $0.1 \lesssim EI^* \lesssim 1$. Flaps with $EI^* \gtrsim 1$ (relatively stiff) produced meandering jets similar to those produced by a rigid pitching foil and $EI^* \lesssim 0.1$ (low-stiffness) flaps produced spread-out jets.

The creation of unidirectional jet and thrust in a quiescent ambient is analogous to that obtained during hovering, for example, by a bird or an insect. The motion, pure pitching (just rotary oscillations), of our foil is much simpler than the complex wing kinematics in birds and insects (Ellington 1984) and can be perhaps exploited in micro aerial vehicles to produce hovering motion. The flexible foil if oriented vertically can produce a force in the upward direction that would exactly balance its weight. For design, this study provides guidelines to choose the flaps with appropriate EI^* values, and also, the required thrust coefficients.

Acknowledgements

We are indebted to Professor R. Narasimha for critical comments, and Professor G. L. Brown, Professor T. J. Pedley and Dr S. S. Diwan for fruitful suggestions. We are grateful to Dr M. R. Cholemari for the help on PIV measurements. We are thankful to anonymous referees for thoughtful comments that helped to improve the manuscript. Financial support from NRB and AOARD, AFOSR is gratefully acknowledged.

Supplementary material and movies

Supplementary material and movies are available at http://dx.doi.org/10.1017/jfm.2014.480.

REFERENCES

ANDERSON, J. M., STREITLIEN, K., BARRETT, D. S. & TRIANTAFYLLOU, M. S. 1998 Oscillating foils of high propulsive efficiency. *J. Fluid Mech.* **360**, 41–72.

BOHL, D. G. & KOOCHESFAHANI, M. M. 2009 MTV measurements of the vortical field in the wake of an airfoil oscillating at high reduced frequency. *J. Fluid Mech.* **620**, 63–88.

CLEAVER, D. J., WANG, Z. & GURSUL, I. 2012 Bifurcating flows of plunging aerofoils at high Strouhal numbers. *J. Fluid Mech.* **708**, 349–376.

DABIRI, J. O. 2005 On the estimation of swimming and flying forces from wake measurements. *J. Expl Biol.* **208**, 3519–3532.

DANIEL, T. L. & COMBES, S. A. 2002 Flexible wings and fins: Bending by inertial or fluid-dynamic forces? *Integr. Compar. Biol.* **42**, 1044–1049.

DAS, P., GOVARDHAN, R. N. & ARAKERI, J. H. 2013 Effect of hinged leaflets on vortex pair generation. *J. Fluid Mech.* **730**, 626–658.

DEWEY, P. A., BOSCHITSCH, B. M., MOORED, K. W., STONE, H. A. & SMITS, A. J. 2013 Scaling laws for the thrust production of flexible pitching panels. *J. Fluid Mech.* **732**, 29–46.

DEWEY, P. A., CARRIOU, A. & SMITS, A. J. 2012 On the relationship between efficiency and wake structure of a batoid-inspired oscillating fin. *J. Fluid Mech.* **691**, 245–266.

ELDREDGE, J. D., TOOMEY, J. & MEDINA, A. 2010 On the roles of chord-wise flexibility in a flapping wing with hovering kinematics. *J. Fluid Mech.* **659**, 94–115.

VON ELLENRIEDER, K. D. & POTHOS, S. 2008 PIV measurements of the asymmetric wake of a two-dimensional heaving hydrofoil. *Exp. Fluids* **44**, 733–745.

ELLINGTON, C. P. 1984 The aerodynamics of hovering insect flight. III. Kinematics. *Phil. Trans. R. Soc. Lond.* B **305**, 41–78.

FREYMUTH, P. 1990 Thrust generation by an airfoil in hover modes. *Exp. Fluids* **9**, 17–24.

GODOY-DIANA, R., AIDER, J. & WESFREID, J. E. 2008 Transition in the wake of a flapping foil. *Phys. Rev.* E **77**, 0163081.

GODOY-DIANA, R., MARAIS, C., AIDER, J. & WESFREID, J. E. 2009 A model for the symmetry breaking of the reverse Bénard–von Kármán vortex street produced by a flapping foil. *J. Fluid Mech.* **622**, 23–32.

GUSTAFSON, K., LEBEN, R. & MCARTHUR, J. 1992 Lift and thrust generation by an airfoil in hover modes. *Comput. Fluid Dyn. J.* **1**, 47–57.

HEATHCOTE, S. & GURSUL, I. 2007 Jet switching phenomenon for a periodically plunging airfoil. *Phys. Fluids* **19**, 0271041.

HEATHCOTE, S., MARTIN, D. & GURSUL, I. 2004 Flexible flapping airfoil propulsion at zero freestream velocity. *AIAA J.* **42**, 2196–2204.

KANG, C. K., AONO, H., CESNIK, C. E. S. & SHYY, W. 2011 Effects of flexibility on the aerodynamic performance of flapping wings. *J. Fluid Mech.* **689**, 32–74.

LAI, J. C. S. & PLATZER, M. F. 2001 Characteristics of a plunging airfoil at zero freestream velocity. *AIAA J.* **39**, 531–534.

LEWIN, G. C. & HAJ-HARIRI, H. 2003 Modelling thrust generation of a two-dimensional heaving airfoil in a viscous flow. *J. Fluid Mech.* **492**, 339–362.

MARAIS, C., THIRIA, B., WESFREID, J. E. & GODOY-DIANA, R. 2012 Stabilizing effect of flexibility in the wake of a flapping foil. *J. Fluid Mech.* **710**, 659–669.

SHINDE, S. Y. 2012 Creation of an orderly jet and thrust generation in quiescent fluid from an oscillating two-dimensional flexible foil. PhD thesis, Indian Institute of Science, Bangalore, India, Department of Mechanical Engineering.

SHINDE, S. Y. & ARAKERI, J. H. 2013 Jet meandering by a foil pitching in quiescent fluid. *Phys. Fluids* **25**, 041701.

SHUKLA, S., GOVARDHAN, R. N. & ARAKERI, J. H. 2013 Dynamics of a flexible splitter plate in the wake of a circular cylinder. *J. Fluids Struct.* **41**, 127–134.

SHYY, W., AONO, H., CHIMAKURTHI, S. K., TRIZILA, P., KANG, C. K., CESNIK, C. E. S. & LIU, H. 2010 Recent progress in flapping wing aerodynamics and aeroelasticity. *Prog. Aerosp. Sci.* **46**, 284–327.

SHYY, W., BERG, M. & LJUNGQVIST, D. 1999 Flapping and flexible wings for biological and micro air vehicles. *Prog. Aerosp. Sci.* **35**, 455–505.

TRIANTAFYLLOU, M. S., TECHET, A. H. & HOVER, F. S. 2004 Review of experimental work in biomimetic foils. *IEEE J. Ocean. Engng* **29**, 585–594.

TRIANTAFYLLOU, M. S., TRIANTAFYLLOU, G. S. & YUE, D. K. P. 2000 Hydrodynamics of fishlike swimming. *Annu. Rev. Fluid Mech.* **32**, 33–53.

WANG, Z. J. 2000 Two-dimensional mechanism for insect hovering. *Phys. Rev. Lett.* **85**, 2216–2219.

WOOTTON, R. J. 1999 Invertebrate paraxial locomotory appendages: design, deformation and control. *J. Expl Biol.* **202**, 3333–3345.